


# Strain modulation of second harmonic generation in new tetrahedral transition metal dichalcogenide monolayers

Hu Chen(陈虎), Shi-Qi Li(李仕琪), Yuqing Wu(吴雨晴), Xiaozhendong Bao(鲍晓振东), Zhijie Lei(雷志杰), Hongsheng Liu(柳洪盛), Yuee Xie(谢月娥), Junfeng Gao(高峻峰), Yuanping Chen(陈元平), and Xiaohong Yan(颜晓红)

**Citation:**Chin. Phys. B, 2025, 34 (**8**): 084206. DOI: 10.1088/1674-1056/addaa3
http://cpb.iphy.ac.cn; http://iopscience.iop.org/cpb

**What follows is a list of articles you may be interested in**

---

## Simultaneous second and third harmonics generation in periodically poled lithium niobate: Coupling and competition

Junming Liu(刘峻铭), Liqiang Liu(刘励强), Lihong Hong(洪丽红), and Zhiyuan Li(李志远)
Chin. Phys. B, 2025, 34 (**8**): 084203. DOI: 10.1088/1674-1056/add24a

## Heterogeneous integration of silicon nitride photonics and CVD-grown $WS_2$ for second harmonic generation

Xuhang Jia(贾旭航), Bangren Xu(许邦仁), Jieyi Luo(罗劼舣), Ning Liu(刘宁), Yuhang Wang(王宇航), Biyuan Zheng(郑弼元), Wei Xu(徐威), and Ken Liu(刘肯)
Chin. Phys. B, 2025, 34 (**7**): 074205. DOI: 10.1088/1674-1056/adc7f7

## A global model of intensity autocorrelation to determine laser pulse duration

Yufei Peng(彭雨菲), Liqiang Liu(刘励强), Lihong Hong(洪丽红), and Zhiyuan Li(李志远)
Chin. Phys. B, 2024, 33 (**5**): 054207. DOI: 10.1088/1674-1056/ad1c57

## Phase-matched second-harmonic generation in hybrid polymer-LN waveguides

Zijie Wang(王梓杰), Bodong Liu(刘伯东), Chunhua Wang(王春华), and Huakang Yu(虞华康)
Chin. Phys. B, 2022, 31 (**10**): 104208. DOI: 10.1088/1674-1056/ac6edc

## Second harmonic generation from precise diamond blade diced ridge waveguides

Hui Xu(徐慧), Ziqi Li(李子琦), Chi Pang(逄驰), Rang Li(李让), Genglin Li(李庚霖), Sh. Akhmadaliev, Shengqiang Zhou(周生强), Qingming Lu(路庆明), Yuechen Jia(贾曰辰), and Feng Chen(陈峰)
Chin. Phys. B, 2022, 31 (**9**): 094209. DOI: 10.1088/1674-1056/ac5242

---

**SPECIAL TOPIC — Artificial intelligence and smart materials innovation: From fundamentals to applications**

# Strain modulation of second harmonic generation in new tetrahedral transition metal dichalcogenide monolayers

Hu Chen(陈虎)[1,3], Shi-Qi Li(李仕琪)[1,3,†], Yuqing Wu(吴雨晴)[1,3], Xiaozhendong Bao(鲍晓振东)[1,3], Zhijie Lei(雷志杰)[1,3], Hongsheng Liu(柳洪盛)[2], Yuee Xie(谢月娥)[1,3,‡], Junfeng Gao(高峻峰)[2,§], Yuanping Chen(陈元平)[1,3], and Xiaohong Yan(颜晓红)[1,3]

[1] *School of Physics and Electronic Engineering, Jiangsu University, Zhenjiang* 212013, *China*
[2] *Laboratory of Materials Modification by Laser, Ion and Electron Beams, Ministry of Education, Dalian University of Technology, Dalian* 116024, *China*
[3] *Quantum Sensing and Agricultural Intelligence Detection Engineering Center of Jiangsu Province, Zhenjiang* 212013, *China*

(Received 26 March 2025; revised manuscript received 16 May 2025; accepted manuscript online 20 May 2025)

Designing novel two-dimensional structures and precisely modulating their second harmonic generation (SHG) attributes are key to advancing nonlinear photonic technologies. In this work, through first-principles calculations, we propose a novel tetrahedral phase of transition metal dichalcogenides (TMDs) and validate its structural feasibility in a family of compounds, i.e., $ZX_2$ ($Z$ = Ti, Zr, Hf; $X$ = S, Se, Te). Cohesive energy and phonon dispersion calculations further demonstrate that eight of nine possible $ZX_2$ monolayers are dynamically stable. All the $ZX_2$ monolayers exhibit pronounced out-of-plane SHG with nonlinear susceptibility components reaching the order of $10^2$ pm/V. Strain engineering imposes a profound influence on the SHG response of $ZX_2$ monolayers by reducing symmetry and modifying nonlinear susceptibility components. The redshift and significant enhancement of the prominent peak in SHG spectra are also revealed due to strain-induced charge redistribution and band gap reduction. Intriguingly, strain-driven nonlinear optical switching effects are realized in the $ZX_2$ monolayers, with a reversible switching of SHG component ordering under tensile and compressive strain. In such a case, the anisotropic SHG pattern transforms from fourfold to twofold symmetry under the strain. Our work demonstrates the efficacy of strain engineering in precisely enhancing SHG, paving the way for the integration of novel TMD structures into tunable and flexible nonlinear optical devices.

**Keywords:** second harmonic generation, strain modulation, transition metal dichalcogenides, phase

**PACS:** 42.65.–k, 42.65.An, 73.22.–f, 42.65.Ky

**DOI:** 10.1088/1674-1056/addaa3 **CSTR:** 32038.14.CPB.addaa3

## 1. Introduction

Second harmonic generation (SHG), as a fundamental second-order nonlinear optical (NLO) response, has become a cornerstone of modern photonics,[1–5] with critical applications in various photonic devices including pulsed lasers,[6] optical switches,[7] optical modulators,[8] photodetectors,[9] and frequency converters.[10,11] Beyond photonic applications, SHG techniques have also shown significant potential in molecular detection,[12] biosensing, and food analysis,[13,14] due to their higher chemical selectivity and greater environmental adaptability compared to traditional nonlinear optical methods (e.g., surface-enhanced raman spectroscopy[15–19]). Two-dimensional (2D) materials provide an ideal platform for SHG applications due to their ultrafast broadband optical response,[20,21] inherently satisfied phase-matching,[22,23] and strong second-order nonlinearities.[24–26]

As a typical representative of 2D materials, transition metal dichalcogenides (TMDs)[27,28] exhibit distinct advantages in nonlinear optics due to their unique structural and optical properties.[29,30] TMDs are composed of elements spanning almost the entire periodic table, forming a vast library of 2D materials with diverse properties and tunable functionalities.[31,32] Besides, TMDs exhibit multiple phase structures, including the semiconducting 2H phase,[33] metallic 1T phase,[33] semimetallic 1T′[34] and Td phase,[35] each imparting distinct electrical and optical characteristics, providing diverse candidates for SHG applications. 2H-phase TMDs exhibit exceptional nonlinear optical responses with substantial second-order nonlinear susceptibility, primarily attributed to their non-centrosymmetric crystal structure.[36,37] Investigating novel structural phases of TMDs is essential for expanding the structural and electronic diversity of this material family. Despite differences in stoichiometry, TMDs and transition metal monochalcogenides (TMCs) share key physicochemical features, including layered structures with anisotropic bonding, a common three-layer atomic motif, and similar d-orbital configurations.[38] These similarities result in comparable responses to external stimuli and give rise to anal-

†Corresponding author. E-mail: shiqili@ujs.edu.cn
‡Corresponding author. E-mail: yueex@ujs.edu.cn
§Corresponding author. E-mail: gaojf@dlut.edu.cn

© 2025 Chinese Physical Society and IOP Publishing Ltd. All rights, including for text and data mining, AI training, and similar technologies, are reserved.

ogous electronic phenomena such as correlation effects and topological phases.[39] Inspired by the existence of tetrahedral structures in TMCs,[39] proposing and exploring a similar phase in TMDs could reveal unconventional electronic, optical, and mechanical properties distinct from the well-known 1T, 2H, and 1T′ phases.

SHG response highly relies on lattice symmetry and can only occur in noncentrosymmetric structures.[1,2] Modulating the SHG response in 2D materials is essential for enhancing nonlinear conversion efficiency and optimizing the performance of NLO devices. Common strategies,[40,41] for modulation and enhancement of the SHG response include heterostructure engineering,[29,42] defect engineering,[3] external electric and magnetic field regulation,[43] and strain engineering.[44,45] Among these methods, strain engineering is highly effective and versatile, enables continuous and reversible control over SHG without introducing defects or altering chemical composition.[46,47] However, the mechanisms underlying strain-induced modulation of second-order nonlinear susceptibility dispersions and anisotropic SHG intensity patterns in TMD structures remain insufficiently explored.

In this work, we propose eight stable $ZX_2$ tetrahedral monolayers and explore their electronic and SHG responses under varying strain. Cohesive energy and phonon dispersion analyses confirm that eight of nine possible $ZX_2$ structures exhibit dynamic stability. All monolayers exhibit pronounced out-of-plane SHG with two independent second-order nonlinear susceptibility components. Strain engineering significantly modifies the SHG response by reducing symmetry, disrupting tensor component equivalence, and introducing new nonlinear susceptibility elements. Charge redistribution and band gap reduction under strain induce a redshift and substantial enhancement of the prominent peaks in SHG spectra. Furthermore, strain modulates nonlinear susceptibility anisotropy, enabling a reversible switching of SHG component ordering under tensile and compressive strain, thus realizing a strain-driven nonlinear optical switching effect. Notably, the anisotropic SHG pattern transitions from fourfold to twofold symmetry under strain.

## 2. Method

All calculations were performed using the Vienna *ab initio* simulation package (VASP),[48,49] based on density functional theory (DFT). The Perdew–Burke–Ernzerhof (PBE) functional within the generalized gradient approximation (GGA) was employed as the exchange–correlation potential,[50,51] with a plane-wave cutoff energy of 500 eV. The interaction between valence electrons and atomic cores was modeled utilizing the projector-augmented wave (PAW) method.[52] Structural optimizations were carried out until the Hellmann–Feynman forces on all atoms were reduced below 0.01 eV/Å, with an energy convergence criterion of $1 \times 10^{-6}$ eV between successive ionic relaxation steps. The vacuum layer thickness was set to 18 Å to prevent the interactions between adjacent image layers. Phonon spectra were obtained via the finite displacement method as executed in the PHONOPY package.[53,54] To address the underestimation of the band gap by the PBE functional, Heyd–Scuseria–Ernzerhof (HSE06) hybrid functional was used to yield accurate band structures.[55] The Brillouin zone integrations were performed using a Monkhorst–Pack $k$-point mesh of $25\times25\times1$. For the electronic structure calculations, a total of 82 $k$ points were employed along the high-symmetry paths.

Aversa and Sipe initially derived expressions for the second-order nonlinear susceptibility using a length-gauge framework,[56] which were later reformulated by Rashkeev, to incorporate all symmetry contributions.[57] The second-order nonlinear susceptibility $\chi^{(2)}_{abc}(-2\omega,\omega,\omega)$ was calculated based on the independent particle approximation considering pure interband transition contributions $\chi^{(2)}_{\text{inter}}(-2\omega,\omega,\omega)$, intraband transition processes $\chi^{(2)}_{\text{intra}}(-2\omega,\omega,\omega)$, and the modulation of interband terms by intraband terms $\chi^{(2)}_{\text{mod}}(-2\omega,\omega,\omega)$.[58,59] Additionally, the scissor approximation, defined as the difference between the PBE and HSE06 band gaps, was applied to account for the missing many-body effects in the SHG calculations.[60] To obtain reliable results on the SHG susceptibility, a denser $k$-point mesh of $50\times50\times1$ was adopted and 100 energy bands were considered. The calculation details are shown in Section S1.

## 3. Results and discussion

Semiconductor materials provide a suitable platform for modeling second-harmonic generation (SHG) mechanisms, as their band structures, optical transition matrix elements, and second-order nonlinear susceptibility tensors can be reliably evaluated using first-principles methods such as density functional theory.[57,59,61] Therefore, our study focuses on the semiconducting tetragonal-phase TMDs. It is well-known that materials with an odd total number of valence electrons generally exhibit metallic behavior.[62] Given that the two chalcogen atoms contribute an even number of valence electrons, transition metals with an odd number of valence electrons, including V, Nb, Ta (group VB), Mn, Tc, Re (group VIIB), and Co, Rh, Ir (group VIIIB), were excluded from consideration. This leaves Ti, Zr, and Hf (group IVB), Cr, Mo, and W (group VIB), and Fe, Ru, and Os (group VIIIB) as possible candidates. By systematic first-principles calculations of the electronic band structures (Fig. S2), we found that only the group IVB tetragonal-phase TMDs exhibit semiconducting behavior. As a result, Ti-, Zr-, and Hf-based systems were ultimately selected as the focus of this work.

### 3.1. Structural characteristics, stability, and electronic properties

The geometric structure of monolayer $ZX_2$ ($Z$ = Ti, Zr, Hf; $X$ = S, Se, Te) is illustrated in Figs. 1(a) (top view) and 1(b) (side view). $ZX_2$ adopts a three-atomic-layer $X$–$Z$–$X$ configuration, similar to other transition metal monochalcogenide phases, such as 2H and 1T. In this structure, the transition metal (Ti, Zr, or Hf) is centrally positioned, sandwiched between two chalcogen layers. These materials belong to the tetragonal crystal system with space group $P\bar{4}m2$, characterized by two orthogonal mirror planes parallel to the $yz$- and $xz$-planes, as well as three mutually perpendicular twofold rotational symmetry axes. The relaxed structural parameters, $Z$–$X$ bond lengths, and thicknesses are listed in Table 1. In all monolayers, the bond lengths between the transition metal atom $Z$ and the two chalcogen atoms are equal. Notably, $ZrTe_2$ exhibits the largest lattice constant of 4.31 Å, while the heaviest $HfTe_2$ has the second-largest lattice constant of 4.28 Å, and the lightest $TiS_2$ displays the smallest lattice constant of 3.68 Å. It is also found that for $ZX_2$ structures with a fixed $Z$ atom, a systematic increase in the lattice constant, $Z$–$X$ bond length, and thickness occurs as the chalcogen element varies from S to Se to Te. This trend stems from the decreasing electronegativity and increasing atomic radius of the chalcogen atoms, which weaken the metal-chalcogen bonds and thus lead to progressively longer bond lengths and greater thicknesses of the monolayers.

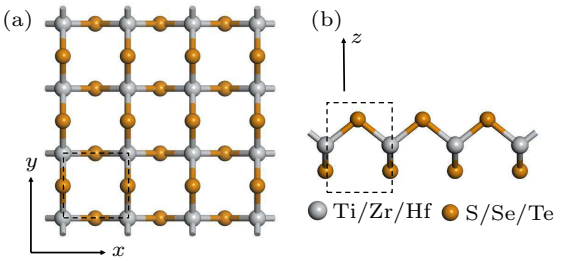



**Fig. 1.** (a) Top and (b) side views of $ZX_2$ ($Z$ = Ti, Zr, Hf and $X$ = S, Se, Te) monolayers. The grey and orange balls represent transition metal and chalcogen atoms, respectively. The unit cell is denoted by the dashed lines.

The thermodynamic stability of these monolayers is evaluated by the cohesive energy ($E_{coh}$), defined as

$$E_{coh} = \frac{E_{total} - (E_Z + 2E_X)}{N}, \quad (1)$$

where $E_{total}$ represents the total energy of the single-layer $ZX_2$, $E_Z$ and $E_X$ denote the energies of isolated transition metal atoms and chalcogen atoms, respectively, and $N$ is the number of atoms in the unit cell. As shown in Table 1, all nine materials exhibit negative cohesive energies, indicating their energetic stability. Notably, $HfS_2$ possesses the lowest cohesive energy (−6.38 eV/atom), indicating it is the most stable among these materials. To further assess the dynamic stability of the studied monolayers, phonon dispersion calculations were performed. The phonon spectra of the nine monolayers are shown in Fig. S3. Except for $ZrSe_2$, the remaining eight structures exhibit no imaginary frequencies, confirming their dynamical stability, resulting in the identification of eight stable $ZX_2$ monolayers.

**Table 1.** The lattice constant (a), $Z$–$X$ bond length ($d_{Z-X}$), thickness, cohesive energy ($E_{Coh}$), and band gaps calculated based on PBE ($E_g^{PBE}$) and HSE06 ($E_g^{HSE06}$) of the nine $Z_2$ monolayers.

| System | $a$ (Å) | $d_{Z-X}$ (Å) | Thickness (Å) | $E_{coh}$ (eV/atom) | $E_g^{PBE}$ (eV) | $E_g^{HSE06}$ (eV) |
|---|---|---|---|---|---|---|
| $TiS_2$ | 3.68 | 2.29 | 2.72 | –5.96 | 1.23 | 1.89 |
| $TiSe_2$ | 3.83 | 2.41 | 2.94 | –5.38 | 0.9 | 1.70 |
| $TiTe_2$ | 4.12 | 2.63 | 3.27 | –4.61 | 0.52 | 0.98 |
| $ZrS_2$ | 3.91 | 2.42 | 2.85 | –6.37 | 1.96 | 2.70 |
| $ZrSe_2$ | 4.04 | 2.55 | 3.11 | –5.75 | 1.53 | 2.21 |
| $ZrTe_2$ | 4.31 | 2.76 | 3.46 | –4.99 | 0.98 | 1.54 |
| $HfS_2$ | 3.88 | 2.41 | 2.86 | –6.38 | 2.22 | 2.85 |
| $HfSe_2$ | 4.01 | 2.54 | 3.11 | –5.72 | 1.78 | 2.35 |
| $HfTe_2$ | 4.28 | 2.75 | 3.45 | –4.93 | 1.61 | 2.38 |

Since second harmonic generation (SHG) is sensitive to the band gap and the PBE functional typically underestimates band gaps, we employed the HSE06 method to obtain more accurate band gap values and band structures for monolayer $ZX_2$ (Fig. S4). The band gap values obtained from HSE06 calculations are 28% to 88% higher compared to PBE results (Table 1). The band structures calculated using both PBE and HSE06 confirm that all nine monolayers exhibit indirect band gaps. The valence band maximum (VBM) is consistently located at the $\Gamma$ point, whereas the conduction band minimum (CBM) appears at the $M$ point in HSE06 results, while it lies along the high-symmetry path between $M$ and $\Gamma$ in PBE calculations. Specifically, $HfS_2$ exhibits the largest band gap of 2.22 eV (PBE) and 2.85 eV (HSE06), whereas $TiTe_2$ possesses the smallest band gap of 0.52 eV (PBE) and 0.98 eV (HSE06). For a fixed $Z$ atom in monolayer $ZX_2$, the band gap decreases as the electronegativity of $X$ decreases (i.e., from S to Se to Te) (Table 1). This can be attributed to the upward shift of

the chalcogen p orbital energies, which raises the VBM while the CBM remains nearly unchanged (Fig. S5). Therefore, all subsequent results are based on HSE06 calculations.

Strain directly induces changes in lattice parameters and can be employed to tailor the electronic properties of these stable $ZX_2$ monolayers. A strain range of ±5% was selected based on experimentally accessible limits and its proven effectiveness in capturing key trends in electronic and nonlinear optical responses without inducing structural instabilities.[46,63,64] The band structures of $ZX_2$ monolayers with different lattice constants corresponding to compressive strain (−5% to −1%), no strain (0%), and tensile strain (1% to 5%) are calculated, as shown in Figs. S6–S11, which reveal the intriguing optical properties of these strained 2D monolayers. The results demonstrate that the application of tensile or compressive strain does not alter the indirect nature of the band gap. The VBM remains located at the $\Gamma$ point, whereas the CBM exhibits strain-dependent shifts, appearing along the $X$–$S$ high-symmetry path under tensile strain and along the $S$–$Y$ high-symmetry path under compressive strain (Figs. S6–S11). The band gaps as a function of strain are presented in Fig. 2. For most monolayers, the band gap displays non-monotonic behavior, with a slight increase observed at ±1% strain, followed by a decrease at strains from ±1% to ±5% (Fig. 2). In contrast, $TiSe_2$ and $HfTe_2$ follow a distinct trend, with their band gaps decreasing consistently as strain increases from 1% to 5% (Figs. 2(a) and 2(c)). Our findings indicate that the electronic band characteristics, including gap magnitude and curvature, exhibit strong sensitivity to strain, enabling strain-mediated tunability of nonlinear optical properties.

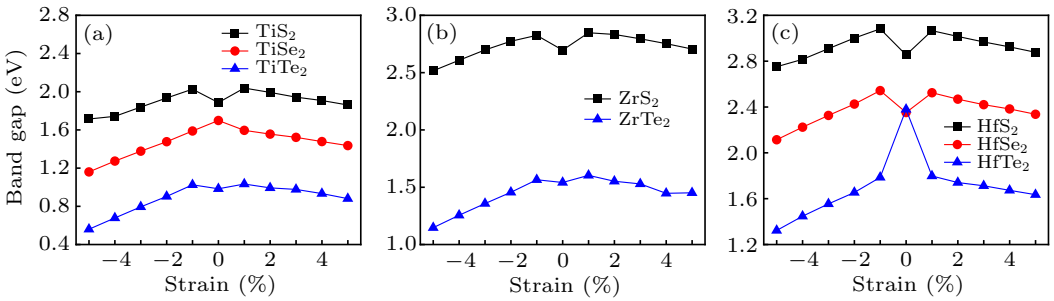



**Fig. 2.** Band gaps of (a) Ti$X_2$, (b) Zr$X_2$, and (c) Hf$X_2$ as a function of strain.

### 3.2. SHG response from Ti$X_2$ monolayers and its strain modulation effect

Taking Ti$X_2$ as an example, we illustrate the effect of strain on the nonlinear optical properties of these 2D materials. The dispersion of second-order nonlinear susceptibility elements under varying strain of Ti$X_2$ is calculated, as shown in Fig. 3. The unstrained Ti$X_2$ crystallizes in the tetragonal system with a space group of $P\bar{4}m2$ and a point group of $D_{2d}$, which lacks an inversion center and thus allows SHG. The second-order nonlinear susceptibility tensor $\chi^{(2)}_{abc}$ of unstrained Ti$X_2$ possesses four out-of-plane nonzero components, including $\chi^{(2)}_{xxz}$, $\chi^{(2)}_{yyz}$, $\chi^{(2)}_{zxx}$, and $\chi^{(2)}_{zyy}$, which satisfy the relations: $\chi^{(2)}_{xxz} = -\chi^{(2)}_{yyz}$, and $\chi^{(2)}_{zxx} = -\chi^{(2)}_{zyy}$ (Figs. 3(b), 3(e) and 3(h)). The presence of a $C_2$ rotational axis in the $xy$-plane imposes strict symmetry constraints that eliminate all in-plane components of the second-order nonlinear susceptibility tensor. All Ti$X_2$ monolayers demonstrate remarkable SHG responses, with out-of-plane components reaching on the order of $10^2$ pm/V, which is several orders of magnitude greater than those of commonly used bulk nonlinear optical materials.[65] As shown in Figs. 3(b), 3(e), and 3(h), the maximum values of $\chi^{(2)}_{xxz}$ for $TiS_2$, $TiSe_2$, and $TiTe_2$ are 287.39 pm/V, 314.71 pm/V, and 684.77 pm/V at 0.93 eV, 0.67 eV, and 0.42 eV, respectively. Meanwhile, the maximum $\chi^{(2)}_{zxx}$ values are 492.52 pm/V, 454.43 pm/V, and 701.40 pm/V at 1.86 eV, 2.19 eV, and 0.80 eV, respectively. Notably, as $X$ transitions from S to Se and then to Te in Ti$X_2$, both $\chi^{(2)}_{xxz}$ and $\chi^{(2)}_{zxx}$ exhibit a gradual increase in magnitude. Furthermore, the positions of the prominent peaks experience a noticeable redshift due to the reduced band gaps (Figs. 3(b), 3(e), and 3(h)). The contributions of interband transitions, intraband transitions, and the modulation of interband terms by intraband terms to the SHG susceptibility were also analyzed (see Fig. S12). For these three monolayers, the $\chi^{(2)}_{xxz}$ and $\chi^{(2)}_{yyz}$ components in the infrared region primarily result from intraband transitions, whereas in the visible region, they arise from both intraband and interband contributions. In contrast, the $\chi^{(2)}_{zxx}$ and $\chi^{(2)}_{zyy}$ components are primarily dictated by interband transitions across the entire spectral range (Fig. S12).

The second-order nonlinear susceptibility $\chi^{(2)}$ exhibits significant changes when 1% and 5% tensile and compressive strains are applied to the three Ti$X_2$ monolayers. First, strain induces a reduction in crystal symmetry, leading to a transformation of the space group from $P\bar{4}m2$ to $Pmm2$. Similar to the unstrained Ti$X_2$ monolayers, the second-order nonlinear susceptibility of strained Ti$X_2$ monolayers includes the $\chi^{(2)}_{xxz}$, $\chi^{(2)}_{yyz}$, $\chi^{(2)}_{zxx}$, and $\chi^{(2)}_{zyy}$ components; however, their original equivalence is disrupted, with $\chi^{(2)}_{xxz} \neq -\chi^{(2)}_{yyz}$ and $\chi^{(2)}_{zxx} \neq -\chi^{(2)}_{zyy}$ (Fig. 3). Additionally, a new $\chi^{(2)}_{zzz}$ component emerges under strain, with a relatively small value of about 30 pm/V in the strained Ti$X_2$

systems. At ±1% strain, the spectra of $\chi^{(2)}_{xxz}$ and $\chi^{(2)}_{zxx}$, as well as $\chi^{(2)}_{yyz}$ and $\chi^{(2)}_{zyy}$, exhibit only minor splitting (Fig. S13), resembling the behavior observed in the unstrained case. However, when the strain increases to ±5%, significant structural deformation leads to a pronounced enhancement of the splitting. For $TiS_2$, $TiSe_2$, and $TiTe_2$ under a tensile strain of 5% (Figs. 3(c), 3(f), and 3(i)), the peak differences between $\chi^{(2)}_{zyy}$ and $\chi^{(2)}_{zxx}$ are 342.85 pm/V, 216.7 pm/V, and 532.5 pm/V, observed at photon energies of 1.86 eV, 1.28 eV, and 0.68 eV, respectively. Meanwhile, the differences between $\chi^{(2)}_{yyz}$ and $\chi^{(2)}_{xxz}$ reach 116.51 pm/V, 166.71 pm/V, and 539.9 pm/V at their respective peak photon energies of 0.91 eV, 0.66 eV, and 0.37 eV (Figs. 3(c), 3(f), and 3(i)). Clearly, upon applying strain, the number of independent components in the second-order nonlinear susceptibility tensor increases from two to five, leading to a significant enhancement in the anisotropy of the SHG response.

Second, strain-driven charge redistribution and band gap reduction lead to a redshift in the prominent peak of SHG spectra, accompanied by a significant enhancement in the SHG response. For instance, under 5% compressive strain, the dominant peak in the $\chi^{(2)}_{zxx}$ spectra of $TiS_2$, $TiSe_2$, and $TiTe_2$ shifts from 1.86 eV, 1.08 eV, and 0.8 eV to 1.35 eV, 0.63 eV, and 0.22 eV, respectively (Figs. 3(a), 3(d), and 3(g)). The nonlinear susceptibility tensor exhibits a notable increase in the infrared region, particularly under compressive strain. For $TiS_2$, the $\chi^{(2)}_{zxx}$ component rises from approximately 100 pm/V to over 200 pm/V within the photon energy range of 0.5–1.5 eV, accompanied by broadening of the peak at 1.8 eV (Fig. 3(a)). In $TiSe_2$, the peak value of $\chi^{(2)}_{xxz}$ doubles from around 300 pm/V to over 600 pm/V, while $\chi^{(2)}_{zxx}$ in the infrared range increases from a few tens of pm/V to over 200 pm/V (Fig. 3(d)). The most pronounced enhancement is observed in $TiTe_2$, where $\chi^{(2)}_{xxz}$ and $\chi^{(2)}_{zxx}$ surge from 700 pm/V to nearly 4000 pm/V under −5% compressive strain (Fig. 3(g)).

Third, strain-engineered nonlinear susceptibility anisotropy reversal is revealed. The SHG component ordering can be reversibly switched under tensile and compressive strain, demonstrating a strain-driven nonlinear optical switching effect. As illustrated in Figs. 3(c), 3(f), and 3(i), under 5% tensile strain, the SHG susceptibility components follow the relationship $\chi^{(2)}_{zyy} > \chi^{(2)}_{zxx}$ and $\chi^{(2)}_{yyz} > \chi^{(2)}_{xxz}$. However, when a 5% compressive strain is applied, the previously established ordering undergoes a complete reversal, resulting in $\chi^{(2)}_{zyy} < \chi^{(2)}_{zxx}$ and $\chi^{(2)}_{yyz} < \chi^{(2)}_{xxz}$ (Figs. 3(a), 3(d), and 3(g)). The ability to modulate the dominance of different SHG components through strain not only enhances the anisotropic characteristics of the system, enabling the design of directional optical devices, but also provides a powerful mechanism for ultrafast optical switching, allowing femtosecond-scale control of optical responses for applications in ultrafast optical communication, quantum optics, and label-free biosensing,[66] including structural imaging and quality monitoring in food systems.[67,68]

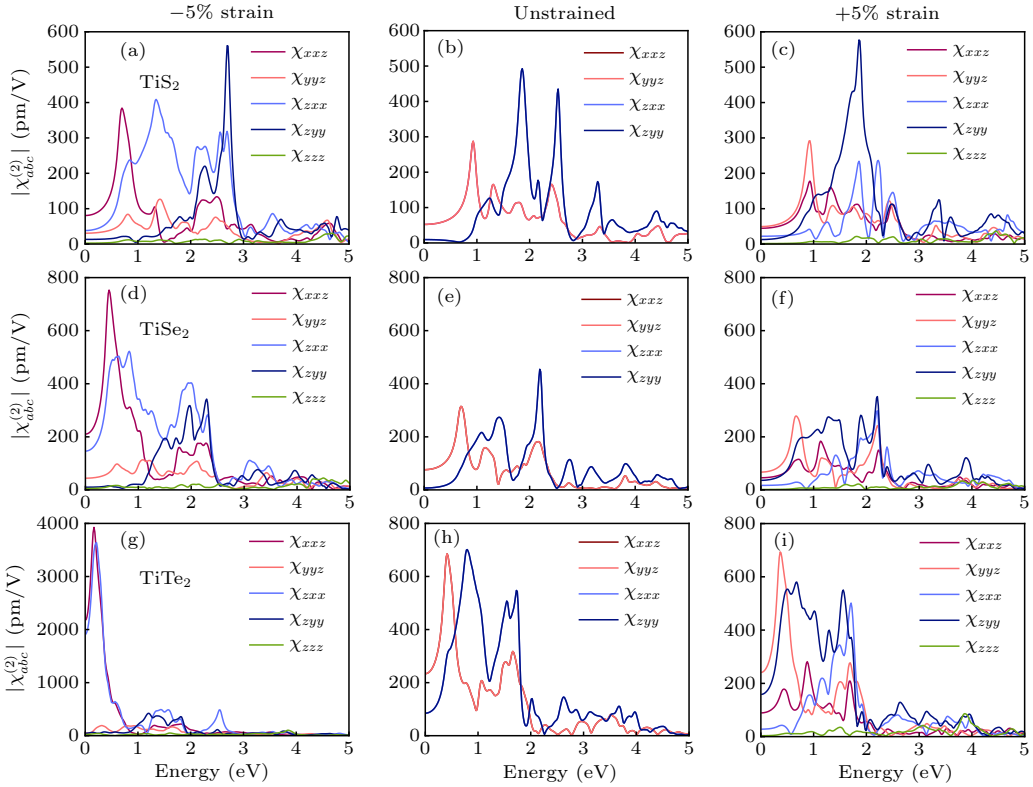



**Fig. 3.** Dispersion of second-order nonlinear susceptibility elements for (a)–(c) $TiS_2$, (d)–(f) $TiSe_2$, and (g)–(i) $TiTe_2$ monolayers under tensile and compressive strains of 5%, respectively.

### 3.3. Comparison of SHG response and strain modulation characteristics in $ZX_2$ monolayers

Except for Ti$X_2$, the SHG responses and strain modulation of the remaining five $ZX_2$ monolayers ($HfS_2$, $HfSe_2$, $HfTe_2$, $ZrS_2$, and $ZrTe_2$) were thoroughly investigated (see Figs. S14 and S15). Due to their $D_{2d}$ space group symmetry, all $ZX_2$ monolayers exhibit four nonzero second-order nonlinear susceptibility components, related by $\chi^{(2)}_{xxz} = -\chi^{(2)}_{yyz}$ and $\chi^{(2)}_{zxx} = -\chi^{(2)}_{zyy}$. Across the photon energy range, the $\chi^{(2)}_{zxx}$ component is consistently larger than $\chi^{(2)}_{xxz}$. Figure 4 presents the maximum values of second-order nonlinear susceptibility elements for both unstrained and strained $ZX_2$. As shown in Fig. 4(a), all unstrained monolayers display exceptional SHG responses, with susceptibility components on the order of $10^2$ pm/V. The SHG spectra also reveal a strong compositional dependence, where the nonlinear susceptibility decreases from Ti to Zr to Hf, with approximate magnitudes of 700 pm/V, 300 pm/V, and 200 pm/V, respectively.

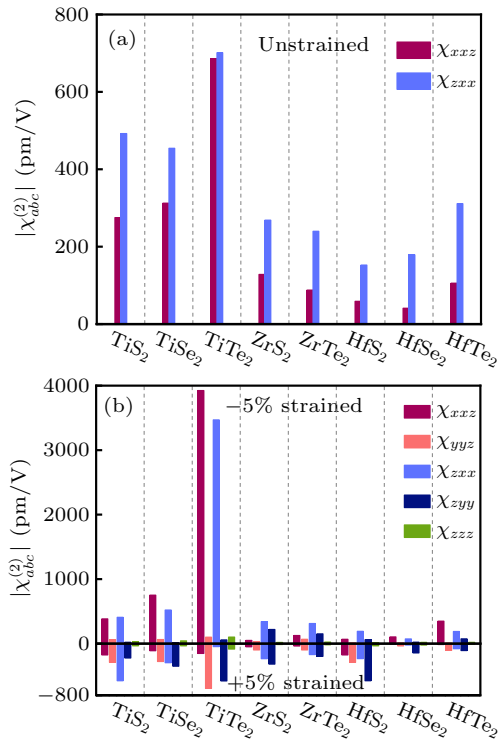



**Fig. 4.** The largest value of second-order nonlinear susceptibility elements for (a) unstrained, (b) −5% strained (upper panel), and +5% strained (lower panel) $ZX_2$ monolayers.

Upon strain application, the crystal symmetry of all $ZX_2$ monolayers reduces to $C_{2v}$, breaking the relations $\chi^{(2)}_{xxz} = -\chi^{(2)}_{yyz}$ and $\chi^{(2)}_{zxx} = -\chi^{(2)}_{zyy}$, and resulting in the emergence of a new $\chi^{(2)}_{zzz}$ component (see Figs. S14 and S15). For most strained $ZX_2$ monolayers, $\chi^{(2)}_{zzz}$ remains around 30 pm/V, except for $TiTe_2$ under −5% strain, where it reaches 85 pm/V. A pronounced strain-induced enhancement of SHG is observed, highly sensitive to elemental composition and most significant in Hf$X_2$ and Ti$X_2$. As illustrated in Fig. 4(b), the maximum values of $\chi^{(2)}_{zxx}$ and $\chi^{(2)}_{xzz}$ dramatically increase to 3925.7 pm/V and 3637.44 pm/V, respectively, representing nearly an order of magnitude enhancement over the unstrained systems. In contrast, tensile strain produces a comparatively weaker enhancement; for example, at 5% tensile strain, $\chi^{(2)}_{zyy}$ in $HfS_2$ increases from 160 pm/V to 600 pm/V. Notably, all $ZX_2$ systems exhibit a significant strain-driven component-switching behavior, with the order of susceptibility components reversing upon tensile or compressive strain application. As shown in Fig. 4(b), the rankings of $\chi^{(2)}_{zyy}$ ($\chi^{(2)}_{yyz}$) and $\chi^{(2)}_{zxx}$ ($\chi^{(2)}_{xxz}$) undergo reversible inversion: under 5% tensile strain, $\chi^{(2)}_{yyz} < \chi^{(2)}_{xxz}$ and $\chi^{(2)}_{zyy} < \chi^{(2)}_{zxx}$, whereas the opposite trend appears under 5% compressive strain. These remarkable strain-dependent responses inherently endow $ZX_2$ monolayers with promising potential for flexible and nonlinear optical device applications.

### 3.4. SHG anisotropic patterns of $ZX_2$ monolayers

Nonlinear SHG responses can be analyzed by illuminating the material with a linearly polarized laser and detecting various polarization components of the emitted SHG signal using an analyzer. Examining the angular dependence, achieved through sample rotation or incident polarization tuning, allows determination of the strain modulation effect on the anisotropic SHG response. The SHG process is governed by the coupling of the optical field $E$ with the second-order nonlinear susceptibility tensor as

$$P_a(2\omega) = \sum_{a,b} \varepsilon_0 \chi^{(2)}_{abc} E_a(\omega) E_b(\omega), \tag{2}$$

where $\varepsilon_0$ is the permittivity of vacuum and $a$, $b$, and $c$ can be $x$, $y$, and $z$, respectively.

The optical field $E$ consists of three components, $E_a$, $E_b$, and $E_c$, incorporating both the incident pump angle $\theta$ and the polarization angle $\alpha$ as

$$\begin{bmatrix} E_a \\ E_b \\ E_c \end{bmatrix} = \begin{bmatrix} E_0 \cos(\theta)\cos(\alpha) \\ E_0 \sin(\alpha) \\ E_0 \sin(\theta)\cos(\alpha) \end{bmatrix}, \tag{3}$$

where $\alpha$ and $\theta$ represent the polarization and incident pump angles, respectively. The parallel component $I_{\parallel}$ and perpendicular component $I_{\perp}$ of the SHG intensity can be described as

$$I^{\parallel}(2\omega) \propto \left(-P_x \cos(\theta) + P_z \sin(\theta)\right)^2, \tag{4}$$

$$I^{\perp}(2\omega) \propto P_y^2. \tag{5}$$

With the calculated second-order nonlinear susceptibility components of unstrained and strained $ZX_2$ and their relationship, the incident angle dependent SHG polarization components as a function of crystal's azimuthal angle and polarization angle for unstrained and strained monolayers can be further denoted as (details are shown in Section S16).

$$I^{\parallel}_{\text{unstrained}} \propto \left[(2\chi_{xxz})\left(\frac{1}{4}\sin(2\theta)\sin(2\varphi)\cos(2\alpha)+\frac{1}{2}\sin(\theta)\cos(2\varphi)\sin(2\alpha)+\frac{1}{4}\sin(2\theta)\sin(2\varphi)\right)\right]^2, \tag{6}$$

$$I^{\parallel}_{\text{strained}} \propto \Big[\chi_{yyz}\cos(\alpha)\cos(\varphi)\sin(\theta)(2\cos(\varphi)\sin(\alpha)+2\cos(\alpha)\cos(\theta)\sin(\varphi)) + \chi_{xxz}\cos(\alpha)\sin(\varphi)\sin(\theta)(2\sin(\alpha)\sin(\varphi)-2\cos(\alpha)\cos(\varphi)\cos(\theta))\Big]^2. \tag{7}$$

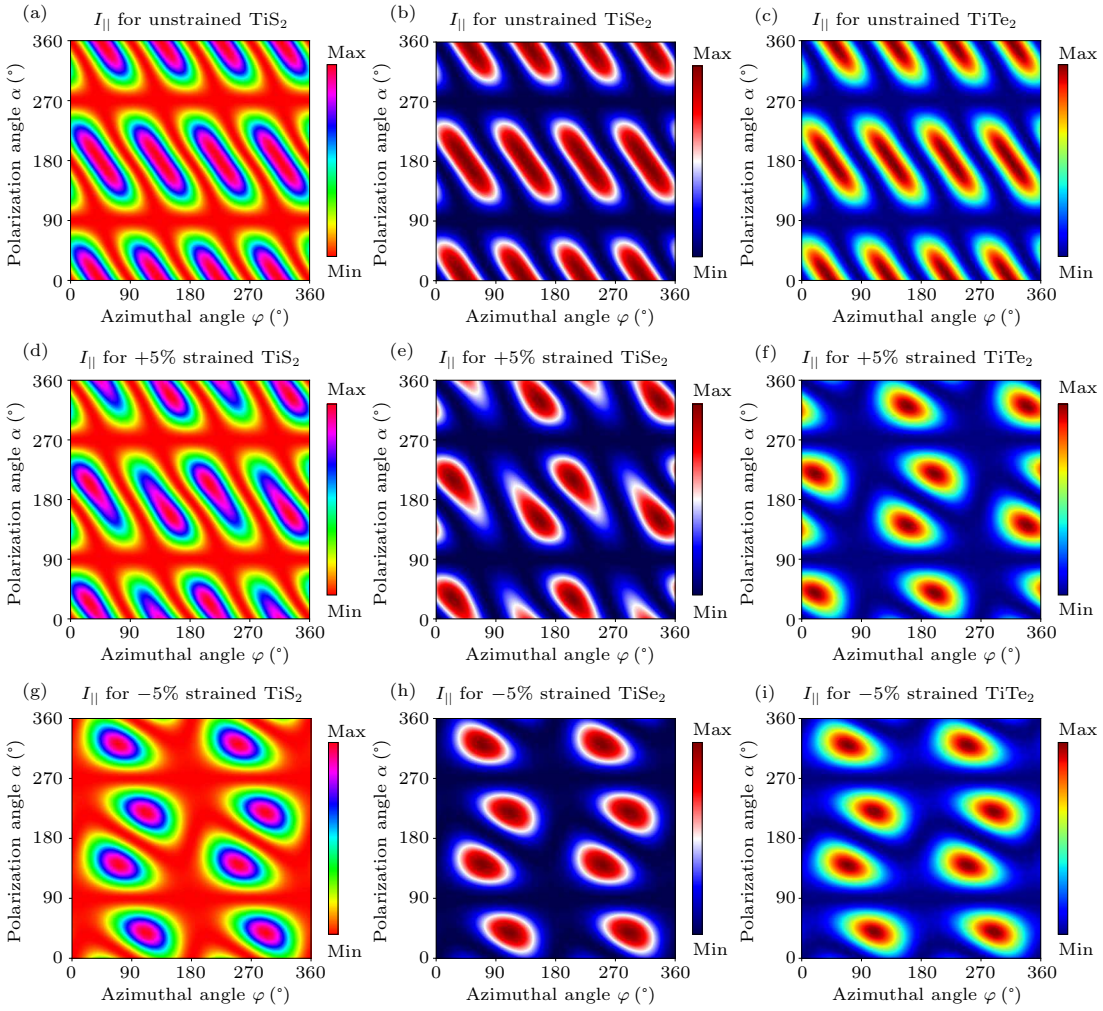



**Fig. 5.** SHG optical heatmap of the normalized parallel components for (a)–(c) unstrained, (d)–(f) 5% tensile strained, and (g)–(i) 5% compressive strained $TiX_2$, with photon energies chosen as 0.9 eV for $TiS_2$, 0.6 eV for $TiSe_2$, and 0.5 eV for $TiTe_2$.

The expressions for the perpendicular polarization components are analogous to those of the parallel components and are provided in Section S16.

By simultaneously varying the azimuthal angle $\varphi$ and the polarization angle $\alpha$, the normalized SHG heatmap for parallel components of $ZX_2$ is obtained, as illustrated in Figs. 5, S17 and S18. For both unstrained and strained $ZX_2$ with the $D_{2d}$ and $C_{2v}$ space groups, the SHG response for these 2D materials can be described by Eqs. (6) and (7). Evidently, the parallel components for the unstrained $ZX_2$ ($I^{\parallel}_{\text{unstrained}}$) are related to the SHG susceptibility tensor element $\chi_{xxz}$, whereas the parallel components for strained $ZX_2$ ($I^{\parallel}_{\text{strained}}$) are related to the now unequal $\chi_{xxz}$ and $\chi_{yyz}$. Figures 5(a)–5(c), S17(a)–S17(c), and S18(a)–S18(c) present the SHG intensity heatmaps of unstrained $ZX_2$. When the polarization angle $\alpha$ is fixed, four equally sized bright spots appear along the $\varphi$ direction, indicating fourfold rotational symmetry. In contrast, under both tensile and compressive strain (Figs. 5(d)–5(i), S17(d)–S17(i), and S18(d)–S18(i)), the heatmaps exhibit twofold rotational symmetry due to the structural point group transition from $D_{2d}$ to $C_{2v}$. The normalized parallel components of the SHG optical heatmap can be further tuned by applying tensile or compressive strain, as strain induces a reversal in the relative ranking of $\chi_{xxz}$ and $\chi_{yyz}$ (Figs. 5(d)–5(i), S17(d)–S17(i), and S18(d)–S18(i)). The optical heatmap of perpendicular SHG intensity components exhibits a similar pattern to that of the parallel components. As shown in Figs. S19–S21, the normalized perpendicular components of the SHG optical heatmap exhibit a transition from fourfold rotational symmetry in unstrained $ZX_2$ monolayers to twofold rotational symmetry under strain.

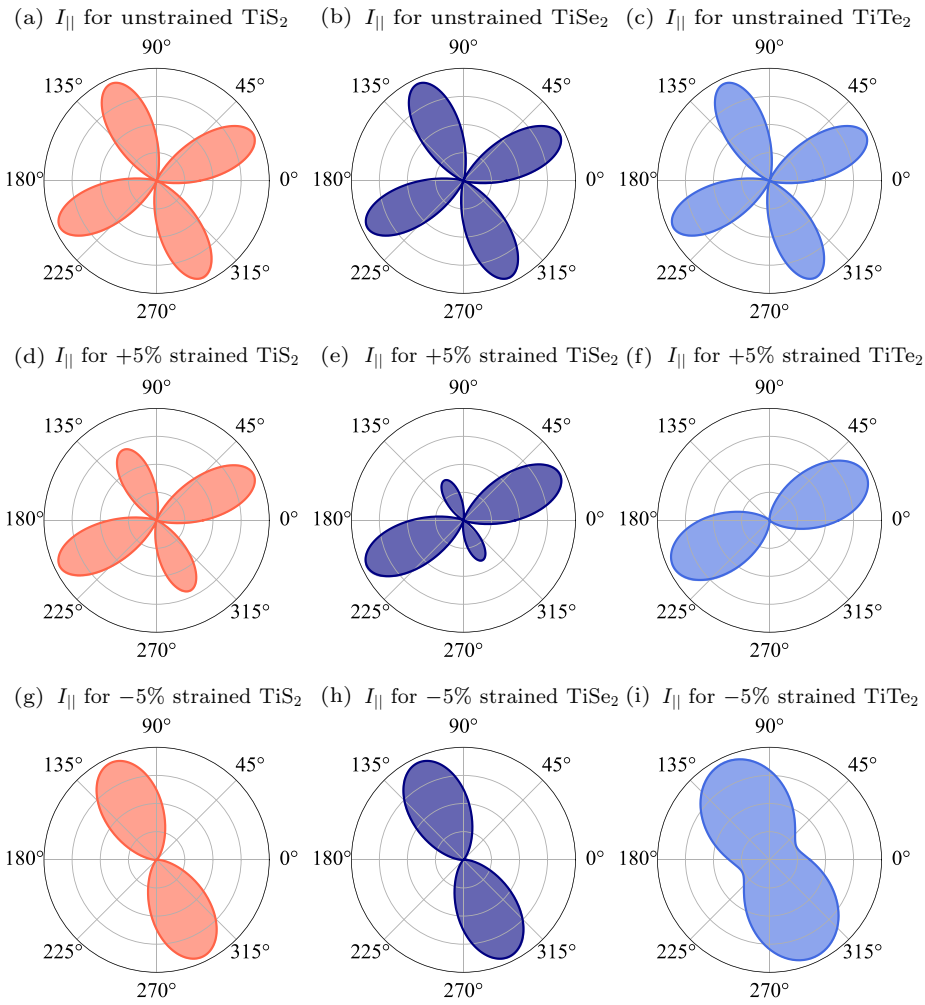



**Fig. 6.** The $\varphi$-dependent anisotropic SHG patterns of parallel component for (a)–(c) unstrained, (d)–(f) 5% tensile strained, and (g)–(i) 5% compressive strained $TiX_2$, with photon energies chosen as 0.9 eV for $TiS_2$, 0.6 eV for $TiSe_2$, and 0.5 eV for $TiTe_2$.

To further elucidate the strain modulation effect on SHG intensity patterns in these 2D monolayers, we examined the $\varphi$-dependent SHG response at a fixed polarization and incident angle ($\alpha = 30°$, $\theta = 45°$). As shown in Figs. 6(a)–6(c), S22(a)–S22(c), and S23(a)–S23(c), the $\varphi$-dependent polar plot patterns for the parallel component of the unstrained monolayers exhibit four equally sized petals, reflecting $C_4$ rotational symmetry, which is markedly different from the typical six-petal pattern observed in hexagonal TMDs.[69] This observation is further supported by the SHG intensity expression, as shown in Eq. (6). When the polarization and incident angles are fixed, the expression simplifies to $I^{\parallel}_{\text{unstrained}} \propto [A\sin(2\varphi+\delta)]^2$, which takes the form of $\sin^2(2\varphi)$. This trigonometric function exhibits four equally sized maxima, consistent with the observed pattern.

With the presence of strain, the tetragonal lattices will be distorted, altering the intrinsic second-order nonlinear coefficients. Correspondingly, a twofold $\varphi$-dependent SHG pattern for $TiX_2$ monolayers under tensile and compressive strains are shown in Figs. 6(d)–6(i), S22(d)–S22(i), and S23(d)–S23(i). This is mainly because strain breaks the original symmetry of the materials, resulting in unequal intrinsic nonlinear susceptibility elements $\chi^{(2)}_{xxz} \neq -\chi^{(2)}_{yyz}$, $\chi^{(2)}_{zxx} \neq -\chi^{(2)}_{zyy}$ and new emergent nonlinear coefficients $\chi^{(2)}_{zzz}$. As shown in Eq. (7), compared with the unstrained case, an additional term independent of $\varphi$ emerges in the SHG intensity expression as the polarization and incident angle are fixed. Consequently, $I^{\parallel}_{\text{strained}}$ can be simplified to the form $I^{\parallel}_{\text{strained}} \propto [A\sin(2\varphi+\delta)+C]^2$, with two primary maxima and two secondary maxima. Consequently, the SHG intensity pattern retains its four-petal configuration, but the petals are redistributed into two pairs of distinct sizes. As shown in Figs. 6(f)–6(h), due to the varying contributions of the five independent second-order nonlinear susceptibility coefficients in the strained structures, the smaller petal pair may completely vanish, revealing a highly anisotropic SHG pattern with responses confined to only two specific directions. The evolution of the SHG polarization pattern for the perpendicular component follows the same trend as that of the parallel component, exhibiting a four-petal structure of equal size in the unstrained monolayers, which transforms into two pairs of equally sized petals under strain (Figs. S24–S26).

## 4. Conclusion

In summary, the strain regulation mechanisms of structural characteristics, electronic properties, and SHG responses in 2D $ZX_2$ monolayers are systematically investigated via comprehensive first-principles calculations. We construct nine tetragonal $ZX_2$ monolayers and identify eight stable monolayers through cohesive energy and phonon calculations. The electronic band structure can be modulated via strain engineering, leading to a strain-dependent SHG response. The application of strain lowers the crystal symmetry, leading to distinctive anisotropic characteristics in the second-order nonlinear susceptibility tensor. First, the original symmetry-constrained relationships $\chi^{(2)}_{xxz} = -\chi^{(2)}_{yyz}$ and $\chi^{(2)}_{zxx} = -\chi^{(2)}_{zyy}$ are disrupted, and new non-zero tensor components $\chi^{(2)}_{zzz}$ emerge. As the strain magnitude increases, these anisotropic features become more pronounced. Second, strain-driven charge redistribution and band gap reduction lead to a redshift in the prominent peak of SHG spectra, accompanied by a significant enhancement in the SHG response. Notably, the most pronounced enhancement is observed in $TiTe_2$, where $\chi^{(2)}_{xxz}$ and $\chi^{(2)}_{zxx}$ surge from 700 pm/V to nearly 4000 pm/V under $-5\%$ compressive strain. Third, strain-engineered nonlinear susceptibility anisotropy reversal is revealed. The SHG component ordering between $\chi^{(2)}_{zyy}$ ($\chi^{(2)}_{yyz}$) and $\chi^{(2)}_{zxx}$ ($\chi^{(2)}_{xxz}$) can be reversibly switched under tensile and compressive strain, demonstrating a strain-driven nonlinear optical switching effect. These findings provide valuable guidance for experimental investigations into SHG behavior and the strain-driven tunability of NLO properties in 2D optoelectronic devices.

## Acknowledgements

This work is supported by the National Natural Science Foundation of China (Grant Nos. 12304220, 12174157, 12074150, and 12374174), the Natural Science Foundation of Jiangsu Province (Grant No. BK20230518), the China Postdoctoral Science Foundation (Grant No. 2023M731383), the College Student Innovation Project (Grant No. 202410299946X), and the Scientific Research Project of Jiangsu University (Grant No. 22A397).

## References

[1] Boyd R W, Gaeta A L and Giese E 2008 *Springer Handbook of Atomic, Molecular, and Optical Physics* (New York, Springer) pp. 1097–1110
[2] Shen Y R 1984 *Principles of Nonlinear Optics* (New York, Wiley-Interscience)
[3] Autere A, Jussila H, Dai Y, Wang Y, Lipsanen H and Sun Z 2018 *Adv. Mater.* **30** 1705963
[4] Huang W, Xiao Y, Xia F, Chen X and Zhai T 2024 *Adv. Funct. Mater.* **34** 2310726
[5] Khan A R, Zhang L, Ishfaq K, Ikram A, Yildrim T, Liu B, Rahman S and Lu Y 2021 *Adv. Funct. Mater.* **32** 2105259
[6] Keller U 2003 *Nature* **424** 831
[7] Chang D E, Vuletić V and Lukin M D 2014 *Nat. Photonics* **8** 685
[8] Elshaari A W, Büyüközer E, Zadeh I E, Lettner T, Zhao P, Schöll E, Gyger S, Reimer M E, Dalacu D and Poole P J 2018 *Nano Lett.* **18** 7969
[9] Nabet B 2023 *Photodetectors: Materials, Devices and Applications* (Cambridge, Woodhead Publishing)
[10] Samanta G, Fayaz G, Sun Z and Ebrahim-Zadeh M 2007 *Opt. Lett.* **32** 400
[11] Bo Y, Geng A, Bi Y, Sun Z, Yang X, Peng Q, Li H, Li R, Cui D and Xu Z 2006 *Appl. Opt.* **45** 2499
[12] Asadipour B, Beaurepaire E, Zhang X, Chessel A, Mahou P, Supatto W, Schanne-Klein M C and Stringari C 2024 *Biophys. J.* **123** 463
[13] Watanabe T M, Maeda Y, Shioi G, Miyazaki K and Fujita H 2025 *J. Food Eng.* **391** 112422
[14] Brüggemann D A, Brewer J, Risbo J and Bagatolli L 2010 *Food Biophys.* **5** 1
[15] Sun Y, Zhai X, Xu Y, Liu C, Zou X, Li Z, Shi J and Huang X 2021 *Food Control* **122** 107772
[16] Zhai W, You T, Ouyang X and Wang M 2021 *Compr. Rev. Food Sci. Food Saf.* **20** 1887
[17] Chen Z, Sun Y, Shi J, Zhang W, Zhang X, Huang X, Zou X, Li Z and Wei R 2022 *Food Chem.* **370** 131276
[18] Zhu J, Agyekum A A, Kutsanedzie F Y, Li H, Chen Q, Ouyang Q and Jiang H 2018 *Lwt* **97** 760
[19] Zhu J, Jiang X, Rong Y, Wei W, Wu S, Jiao T and Chen Q 2023 *Food Chem.* **414** 135705
[20] Bonaccorso F, Sun Z, Hasan T and Ferrari A C 2010 *Nat. Photonics* **4** 611
[21] Liu M, Yin X, Ulin-Avila E, Geng B, Zentgraf T, Ju L, Wang F and Zhang X 2011 *Nature* **474** 64
[22] Ciattoni A, Marini A, Rizza C and Conti C 2018 *Light Sci. Appl.* **7** 5
[23] Zhao M, Ye Z, Suzuki R, Ye Y, Zhu H, Xiao J, Wang Y, Iwasa Y and Zhang X 2016 *Light Sci. Appl.* **5** e16131
[24] Wang H and Qian X 2017 *Nano Lett.* **17** 5027
[25] LI S Q, He C, Liu H, Zhao L, Xu X, Chen M, Wang L, Zhao J and Gao J 2022 *Adv. Opt. Mater.* **10** 2200076
[26] Zhao B J, Zhao J L and Gan X T 2024 *Chin. Phys. Lett.* **41** 104201
[27] Manzeli S, Ovchinnikov D, Pasquier D, Yazyev O V and Kis A 2017 *Nat. Rev. Mater.* **2** 17033
[28] Choi W, Choudhary N, Han G H, Park J, Akinwande D and Lee Y H 2017 *Materials Today* **20** 116
[29] Strasser A, Wang H and Qian X 2022 *Nano Lett.* **22** 4145
[30] Seyler K L, Schaibley J R, Gong P, Rivera P, Jones A M, Wu S, Yan J, Mandrus D G, Yao W and Xu X 2015 *Nat. Nanotechnol.* **10** 407
[31] Voiry D, Mohite A and Chhowalla M 2015 *Chem. Soc. Rev.* **44** 2702
[32] Fu Q, Han J, Wang X, Xu P, Yao T, Zhong J, Zhong W, Liu S, Gao T and Zhang Z 2021 *Adv. Mater.* **33** 1907818
[33] Friedman A L, Hanbicki A T, Perkins F K, Jernigan G G, Culbertson J C and Campbell P M 2017 *Sci. Rep.* **7** 3836
[34] Tan S J, Abdelwahab I, Ding Z, Zhao X, Yang T, Loke G Z, Lin H, Verzhbitskiy I, Poh S M and Xu H 2017 *J. Am. Chem. Soc.* **139** 2504
[35] Ma X, Guo P, Yi C, Yu Q, Zhang A, Ji J, Tian Y, Jin F, Wang Y and Liu K 2016 *Phys. Rev. B* **94** 214105
[36] He C, Zhao Q, Huang Y, Zhu L, Zhang S, Bai J and Xu X 2019 *J. Phys. Chem. Lett.* **10** 2090
[37] Kumar N, Najmaei S, Cui Q, Ceballos F, Ajayan P M, Lou J and Zhao H 2013 *Phys. Rev. B* **87** 161403
[38] Tedstone A A, Lewis D J and O'Brien P 2016 *Chem. Mater.* **28** 1965
[39] Zhou X and Rodriguez E E 2017 *Chem. Mater.* **29** 5737
[40] Zhang C P and Miao X Y 2023 *Chin. Phys. Lett.* **40** 124201
[41] Qiao Y, Chen J, Zhou S, Chen J, Jiang S and Yang Y 2024 *Chin. Phys. Lett.* **41** 014205
[42] Zhang A, Qiu S, Zhao L, Liu H, Zhao J and Gao J 2024 *Laser Photonics Rev.* **18** 2300742
[43] An Y Q, Nelson F, Lee J U and Diebold A C 2013 *Nano Lett.* **13** 2104
[44] He C, Wu R, Zhu L, Huang Y, Du W, Qi M, Zhou Y, Zhao Q and Xu X 2022 *J. Phys. Chem. Lett.* **13** 352
[45] He C, Zhao Q, Huang Y, Du W, Zhu L, Zhou Y, Zhang S and Xu X 2020 *Phys. Chem. Chem. Phys.* **22** 21428
[46] Mennel L, Furchi M M, Wachter S, Paur M, Polyushkin D K and Mueller T 2018 *Nat. Commun.* **9** 516
[47] Liang J, Zhang J, Li Z, Hong H, Wang J, Zhang Z, Zhou X, Qiao R, Xu J and Gao P 2017 *Nano Lett.* **17** 7539
[48] Kresse G and Furthmĺler J 1996 *Comput. Mater. Sci.* **6** 15

[49] Kresse G and Furthmüller J 1996 *Phys. Rev. B* **54** 11169
[50] Perdew J P, Burke K and Ernzerhof M 1996 *Phys. Rev. Lett.* **77** 3865
[51] Troullier N and Martins J L 1991 *Phys. Rev. B* **43** 1993
[52] Blöchl P E 1994 *Phys. Rev. B* **50** 17953
[53] Gonze X, Charlier J C, Allan D and Teter M 1994 *Phys. Rev. B* **50** 13035
[54] Giannozzi P, De Gironcoli S, Pavone P and Baroni S 1991 *Phys. Rev. B* **43** 7231
[55] Heyd J, Scuseria G E and Ernzerhof M 2003 *J. Chem. Phys.* **118** 8207
[56] Aversa C and Sipe J E 1995 *Phys. Rev. B* **52** 14636
[57] Rashkeev S N, Lambrecht W R and Segall B 1998 *Phys. Rev. B* **57** 3905
[58] Sipe J and Ghahramani E 1993 *Phys. Rev. B* **48** 11705
[59] Sharma S, Dewhurst J K and Ambrosch-Draxl C 2003 *Phys. Rev. B* **67** 165332
[60] Levine Z H and Allan D C 1991 *Phys. Rev. Lett.* **66** 41
[61] Sipe J and Shkrebtii A 2000 *Phys. Rev. B* **61** 5337
[62] Grundmann M 2006 *The physics of semiconductors* Vol. **13** (New York: Springer)
[63] Horzum S, Sahin H, Cahangirov S, Cudazzo P, Rubio A, Serin T and Peeters F 2013 *Phys. Rev. B* **87** 125415
[64] Rahman S, Yildirim T, Tebyetekerwa M, Khan A R and Lu Y 2022 *ACS Nano* **16** 13959
[65] Eckardt R C, Masuda H, Fan Y X and Byer R L 1990 *IEEE J. Quantum Electron.* **26** 922
[66] Guo Z, Wang M, Barimah A O, Chen Q, Li H, Shi J, El-Seedi H R and Zou X 2021 *Int. J. Food Microbiol.* **338** 108990
[67] Han F, Huang X and Mahunu G K 2017 *Trends Food Sci. Technol.* **59** 37
[68] Xu Y, Hassan M M, Sharma A S, Li H and Chen Q 2023 *Crit. Rev. Food Sci. Nutr.* **63** 486
[69] He C, Zhu L, Huang Y, Du W, Qi M, Zhou Y, Zhao Q and Xu X 2022 *J. Phys. Chem. C* **126** 10584